Available online at www.sciencedirect.com

SciVerse ScienceDirect

Acta Materialia 61 (2013) 2919–2925

Acta MATERIALIA

www.elsevier.com/locate/actamat

Large-scale first-principles determination of anisotropic mechanical properties of magnetostrictive Fe–Ga alloys

Hui Wang [a,b,c,d], Z.D. Zhang [a,b], R.Q. Wu [d], L.Z. Sun [c,*]

[a] Shenyang National Laboratory of Materials Science, Institute of Metal Research, Chinese Academy of Sciences, Shenyang 110016, People's Republic of China

[b] International Centre of Materials Physics, Chinese Academy of Sciences, Shenyang 110016, People's Republic of China

[c] Department of Civil and Environmental Engineering, University of California, Irvine, CA 92697-2175, USA

[d] Department of Physics and Astronomy, University of California, Irvine, CA 92697-4575, USA

Received 29 December 2012; received in revised form 21 January 2013; accepted 22 January 2013

Abstract

Magnetostrictive $Fe_{1-x}Ga_x$ alloys, as a new class of smart materials, have great potential in sensing and actuator applications. However, the fundamental understanding of the anisotropic elastic responses at high Ga concentration remains one of the most challenging problems for the binary alloys. Here, we apply the density functional theory and large-scale ab initio molecular dynamics simulation to investigate the effect of high Ga concentration on the elastic anisotropy of the Fe–Ga alloys with supercell models obtained by non-linear and non-uniform annealing processes. It is demonstrated that the formation of $D0_3$-like structures has an important effect on the softness of the tetragonal shear modulus and a negligible influence on the rhombohedral shear modulus. Meanwhile, the Fe dangling bond to its nearest Ga atoms results in a decrease in the Young's modulus and the negative Poisson's ratio in the [1 1 0] direction. The improved Young's modulus in the [1 1 0] direction compared to that in the [1 0 0] direction is attributed to the different arrangement of the pure Fe layer and the Fe–Ga mixed layer along the [1 1 0] and [1 0 0] axes. Furthermore, the ductility of $Fe_{1-x}Ga_x$ alloys is enhanced at high Ga content, playing a key role in the enhanced magnetostriction.

Keywords: Fe–Ga alloys; Density functional theory; Mechanical property; Anisotropy; Magnetostrictive alloys

1. Introduction

Materials exhibiting a coupling between magnetization and strain are magnetostrictive materials, which play an increasingly important role in various applications ranging from stress- and torque-sensing devices to actuator and energy harvesters [1–3]. Such adaptive materials can change their dimensions under an external magnetic field, and conversely, the magnetic state can be tailored by the application of a mechanical load. Terfenol-D ($Tb_xDy_{1-x}Fe_2$) alloys are well known for their giant magnetostriction up to a few thousands ppm, and have already been used in practical applications in the past few decades [4,5]. Ni_2MnGa Heusler shape memory alloys [6,7] exhibit large strains up to 6%, which primarily stems from a magnetic-field-induced martensitic phase transition. However, the applications of these alloys have been limited owing to their mechanical brittleness and their use of rare-earth elements (in the case of Terfenol-D). Exploration of a new class of materials with combined high magnetostriction and mechanical ductility is indeed needed.

In view of their electronic structure, ductile materials usually consist of metallic elements that form metallic bonds with delocalized electronic states. As one of the Fe-based magnetostrictive materials, $Fe_{1-x}Ga_x$ alloys (Galfenol) exhibit desirable mechanical properties and large tetragonal magnetostriction under a lower magnetic field (150–250 Oe), ideal for sensor and actuator applications [8]. Interdisciplinary research efforts have been dedi-

* Corresponding author. Tel.: +1 949 824 8670; fax: +1 949 824 2117.
E-mail address: lsun@uci.edu (L.Z. Sun).

1359-6454/$36.00
http://dx.doi.org/10.1016/j.actamat.2013.01.046

cated to understand the composition dependence of phase stabilities [9] and the magnetoelastic coupling mechanism of these alloys [10–14]. In particular, the weak elastic stiffness at high Ga concentrations is assigned as one of the primary reasons for the enhancement of magnetostriction of $Fe_{1-x}Ga_x$ [15]. Furthermore, due to the different atomic arrangement in crystallographic axes, single-crystalline $Fe_{1-x}Ga_x$ alloys demonstrate a strong elastic anisotropy [16]. This leads to auxeticity, i.e. negative Poisson's ratio, which is associated with indentation resistance, fracture toughness and damping/sound absorption. A thorough, systematic investigation of the anisotropic mechanical properties of $Fe_{1-x}Ga_x$ alloys is essential to understand the deformation mechanism responsible for the magnetostriction at high Ga concentration, especially near the first magnetostriction peak. However, it is still a challenge to simulate actual materials around $x = 19\%$ through density functional theory (DFT) calculations, due to the size limit of unit-cell models and complex chemical ordering of Ga atoms in the body-centered cubic (bcc) lattice.

In this work, we report the results of anisotropic elastic properties of $Fe_{1-x}Ga_x$ alloys using the DFT-based ab initio molecular dynamics (AIMD) simulation. We observe that the formation of $D0_3$-like structures has an important effect on the softness of tetragonal shear modulus and a negligible influence on the rhombohedral shear modulus. The decrease in the Young's modulus and the negative Poisson's ratio in the [1 1 0] direction can be attributed to the induced Fe dangling bond to its nearest Ga atoms. The calculated anisotropic elastic constants agree well with experimental data reported by different groups. Furthermore, we demonstrate that the enhanced ductility of the alloys with increased Ga content can be explained in terms of the Cauchy pressure and the Pugh's modulus ratio.

2. Computational methodology

2.1. Density functional theory and ab initio molecular dynamics

The molecular dynamics (MD) approach allows simulation of dynamic processes in the framework of Newton's equation of motion. One of the most important aspects of MD simulation is the calculation of the potential energy surface or atomic forces. DFT-based electronic structure calculations can accurately describe the multi-body interaction in condensed matter systems by solving the Kohn–Sham equations self-consistently [17]. Ab initio molecular dynamics, unifying Newton's and Schrödinger's equations, may simulate the finite-temperature dynamic process by using forces computed from DFT calculations without relying on any adjustable parameters [18,19].

We conducted the electronic-structure calculations and structural relaxations of $Fe_{1-x}Ga_x$ alloys using the Vienna Ab-initio Simulation Package (VASP) [20]. The spin-polarized generalized gradient approximation (GGA) was employed to describe the electronic exchange and correlation interaction of electrons, using the Perdew–Burke–Ernzerhof (PBE) functional [21]. We treated Fe-3d4s4p and Ga-3d4s4p as valence states and adopted the projector-augmented wave (PAW) method [22] to represent the effect of the ionic cores. The energy cutoff for plane-wave expansion was set as 400 eV, which is sufficient for Fe–Ga systems according to test calculations. At the end of AIMD steps, we optimize the atomic structure further, with a criterion that the atomic force on each atom becomes weaker than 0.01 eV $Å^{-1}$ and the energy convergence is better than 10^{-5} eV.

For high Ga concentration ($15.6\% < x < 22.7\%$) cases, based on our recent ab initio molecular dynamics simulation [12], we set up 10 initial structures randomly with 128 Fe and Ga atoms taking the bcc lattice sites of the $4 \times 4 \times 4$ cubic supercell for each Ga concentration. We heated the system up to 2000 K, which is far above the melting point of Galfenol (1500 K) for 15 ps. The convergence of the total free energy (~ -770 eV per cell) after 0.5 ps and the calculated Ga–Ga radial pair distribution function (RDF) demonstrates the liquid phase at 2000 K. We further cooled the system down to 500 K with non-uniform and non-linear cooling rates (especially about 10^{12} K s^{-1} near the melting point where the total free energy decreases abruptly) for the recrystallization. The calculated Ga–Ga RDF and the snapshot of atomic arrangement exhibit the crystallized phase at 500 K. The structures were fully relaxed at 0 K. We eventually chose the most energetically favorable atomic configurations for each Ga concentration. As an example, a supercell with 128 atoms for Ga concentration only at 20.3% was illustrated, shown in Fig. 1.

For the integrity of this work, various sized unit cells were applied for $Fe_{1-x}Ga_x$ alloys at different Ga compositions. For low Ga concentration ($x \leqslant 12.5\%$), the 16-atom unit-cell model has proved to be accurate enough to characterize the Ga distribution in $Fe_{1-x}Ga_x$ alloys [10]. Specifically, only one Fe site at the center position (1/2, 1/2, 1/2)

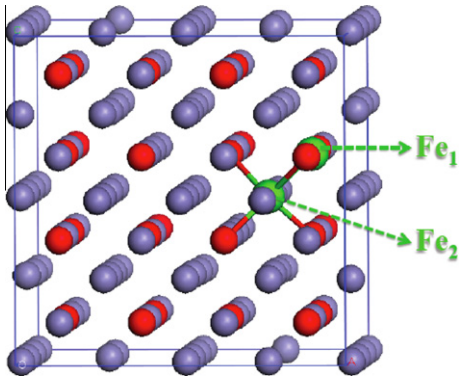

Fig. 1. Atomic configurations for $Fe_{1-x}Ga_x$ alloys at $x = 20.3\%$. The blue and red balls represent Fe and Ga atoms, respectively. The green balls depicted by Fe_1 and Fe_2 represent the Fe atoms in mixed Fe–Ga layer and pure Fe layer, respectively. (For interpretation of the references to color in this figure legend, the reader is referred to the web version of this article.)

and two Fe sites at the original position (0, 0, 0) and center position (1/2, 1/2, 1/2) were replaced by the Ga atoms in the unit cell with 16 atoms, corresponding to Ga-6.25% and Ga-12.5%, respectively, while for high Ga concentration ($12.5 < x \leqslant 22.7\%$), the 128-atom supercell was selected from MD results. A $13 \times 13 \times 13$ Monkhost–Pack and $4 \times 4 \times 4$ gamma-centered k-point mesh in the Brillouin zone [23] was used to evaluate integrals in the reciprocal space for the 16-atom unit cell and 128-atom supercell, respectively. Test calculation of K-point for $Fe_{1-x}Ga_x$ alloys at $x = 20.3\%$ (128-atom supercell) indicates that $4 \times 4 \times 4$ gamma-centered K-point mesh is accurate enough for the total energy and magnetic property calculations with the 128-atom supercell model.

2.2. Determination of elastic constants

In the case of cubic crystalline alloys, symmetry permits the relationship between the stresses and strains to be completely defined with the three elastic constants C_{11}, C_{12} and C_{44}, which can be determined based on the strain-dependent strain energy [24]. In general, with infinitesimal strains (all six strain components e_1, e_2, e_3, e_4, e_5, e_6) applied to distort the lattice within the volume V, the total strain energy U is defined as:

$$U = \frac{V}{2}\sum_{i=1}^{6}\sum_{j=1}^{6} C_{ij}e_i e_j \tag{1}$$

and can be explicitly expressed as:

$$U = \frac{V}{2}\left(C_{11}e_1^2 + C_{11}e_2^2 + C_{11}e_3^2 + 2C_{12}e_1e_2 + 2C_{12}e_1e_3 + 2C_{12}e_2e_3 + C_{44}e_4^2 + C_{44}e_5^2 + C_{44}e_6^2\right) \tag{2}$$

for a cubic symmetric system.

Specifically, for rhombohedral distortion, the six strain components are (0, 0, 0, δ, δ, δ) and the strain energy can be simplified as:

$$U = \frac{3}{2V}C_{44}\delta^2 \tag{3}$$

Similarly, the tetragonal distortion (δ, 0, 0, 0, 0, 0) in the [1 0 0] direction can yield the corresponding strain energy as:

$$U = \frac{1}{2V}C_{11}\delta^2 \tag{4}$$

Furthermore, the bulk modulus B of the lattice is associated with the elastic constants as:

$$B = \frac{C_{11} + 2C_{12}}{3} \tag{5}$$

which can be calculated from the second derivative of the volume-dependent total energy E_{total} as:

$$B = V\left.\frac{d^2E_{total}}{dV^2}\right|_{V=V_0} \tag{6}$$

with V_0 being the lattice volume at equilibrium stage. With the combination of Eqs. (3)–(6), the three independent elastic constants C_{11}, C_{12} and C_{44} can be determined.

Since C_{11}, C_{12} and C_{44} compromise a complete set of elastic constants for a cubic system, the direction-dependent Young's modulus E and Poisson's ratio v can be derived by the following equations:

$$E_{[100]} = \frac{C_{11}R}{C_{11} + C_{12}} \tag{7}$$

$$E_{[110]} = \frac{4C_{44}R}{2C_{44} + R} \tag{8}$$

$$v_{[010]} = \frac{C_{12}}{C_{11} + C_{12}} \tag{9}$$

$$v_{[110]} = \frac{R - 2C_{44}}{R + 2C_{44}} \tag{10}$$

where $R = (C_{11} - C_{12})(C_{11} + 2C_{12})/C_{11}$.

3. Results and discussion

One important factor responsible for the magnetostriction of $Fe_{1-x}Ga_x$ alloys can be attributed to the effect of additional Ga atoms on the mechanical properties of these alloys, such as the tetragonal shear modulus C' ($C' = (C_{11} - C_{12})/2$) and the rhombohedral shear modulus C_{44} for tetragonal and rhombohedral magnetostriction, respectively. In order to obtain these shear constants, the dependence of the total energy on lattice volume, and the strain energy density as a function of either tetragonal strain in the [1 0 0] direction or rhombohedral strain in the [1 1 1] direction, need to be determined first, as demonstrated in Fig. 2. The smoothness of data indicates the high quality and reliability of our calculations, and the anisotropic elastic constants can be acquired by fitting the data with the quadratic polynomials based on Eqs. (3)–(5).

The dependence of the calculated tetragonal and rhombohedral shear constant on Ga concentrations demonstrated a very different behavior, as illustrated in Fig. 3a and b, which generally agrees well with the available experimental data in the literature [14,15,25,26]. Further, C' showed a strong linear dependence of Ga concentration and decreased almost by a factor of five in the range studied here, while C_{44} exhibits weak dependence of Ga concentration, which is also consistent with the form effect corrected results by using the electron-per-atom ratio (e/a) as the common variable [27]. More importantly, to uncover the underlying reasons, detailed studies of the dependence of local chemical structures on shear constants are indeed needed. Previous investigations of the microstructure of $Fe_{1-x}Ga_x$ alloys have been performed close to the first peak in the magnetostriction [28], which reveal the formation of $D0_3$-like structures due to the coherent nature of the A2 matrix and $D0_3$-like structures. Meanwhile, recent theoretical calculations demonstrated that the instability of the $D0_3$ structure can be removed by applying a hydrostatic-type strain of 0.3% [11] or by

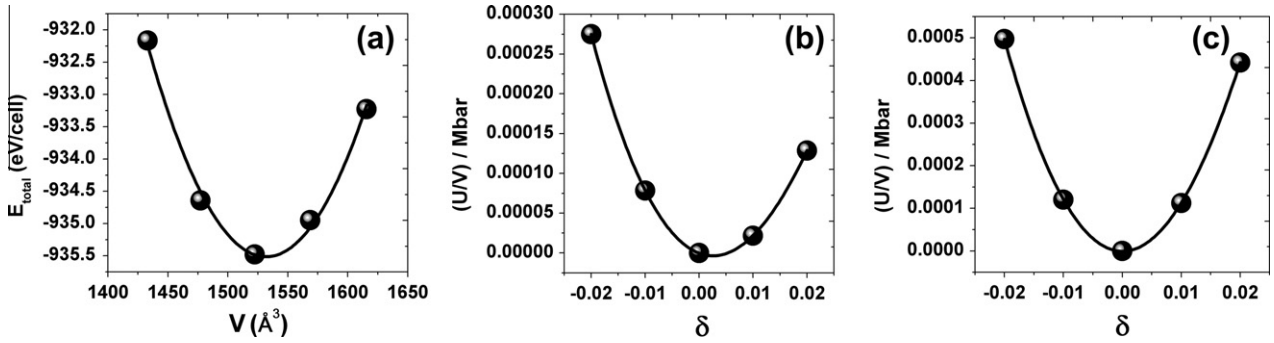

Fig. 2. Quadratic dependence of total energy E_{total} on lattice volume (a) and strain energy density U/V on tetragonal strain (b) and rhombohedral strain (c) for $Fe_{1-x}Ga_x$ at $x = 20.3\%$.

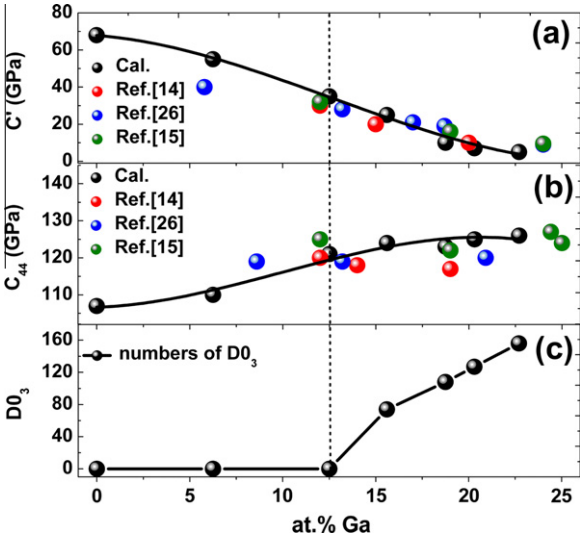

Fig. 3. DFT simulation and experimental data of dependence of (a) tetragonal shear constant C', (b) rhombohedral shear constant C_{44} and (c) local chemical structures, $D0_3$-like structures on the Ga concentration for $Fe_{1-x}Ga_x$ alloys. The vertical dash line indicates the boundary between low and high Ga concentration.

including small pocket of A2 phase throughout the structure [29]. In this work, we calculated the radial distribution function (RDF) and integrated it over the whole supercell to obtain the number of $D0_3$-like structures for each Ga concentration, as depicted in Fig. 3c. As we can see at low Ga concentration (the left side of the vertical dash line in Fig. 3c), no $D0_3$-like structures were observed, indicating that the randomly distributed Ga atoms in the bcc-Fe matrix is probably the main structure in this range, where C' almost decreased to the half value of pure bcc-Fe and C_{44} increased by 15–20%. With the continuous increasing of Ga content, $D0_3$-like structures increased significantly and gradually increased at higher Ga concentration, as shown in the right side of the vertical dash line of Fig. 3c. The linear decreasing of C' is continuous until it reaches non-zero minimum in this range; this is probably due to the fact that the formation of $D0_3$-like structure induced more dangling bonds for Fe atoms adjacent to Ga atoms. Differently, C_{44} is almost insensitive to Ga content and almost kept a constant value between 125 and 130 GPa, which indicate that $D0_3$-like structures have negligible influence on the rhombohedral shear modulus.

To aid engineering application, a more detailed investigation of the mechanical properties of $Fe_{1-x}Ga_x$ alloys, such as Young's modulus and Poisson's ratio, in certain crystallographic axes is needed. Based on Eqs. (7)–(10), the Young's modulus E and Poisson's ratio v can be determined by the anisotropic elastic constants obtained above. As shown in Fig. 4, the AIMD simulation results qualitatively match all the experimental results [22,24] very well, indicating the consistent electronic origin of $Fe_{1-x}Ga_x$ microstructures. As demonstrated in Fig. 4a, the Young's moduli $E_{[100]}$ and $E_{[110]}$ in the directions of [100] and [110] decrease with the increased Ga-composition while $E_{[110]}$ is greater than $E_{[100]}$ indicating an anisotropic elastic response. From Fig. 4b, the Poisson's ratio $v_{[010]}$ in the [010] direction almost keeps as constant, while $v_{[110]}$ in the [110] direction drops from positive to negative at $x = 7\%$ and reaches a negative value of -0.67 at $x = 23\%$, indicating an auxetic response of $Fe_{1-x}Ga_x$ alloys at high Ga concentration.

The anisotropy of the Young's modulus comes from the different arrangement of a pure Fe layer and a Fe–Ga mixed layer in crystallographic axes. As Ga concentration increases, Ga atoms prefer to stay away from each other in the bcc-Fe matrix. Previous theoretical results demonstrate that Fe atoms nearest to Ga atoms (Fe_2 atoms shown in Fig. 1) provide with the largest contribution to magnetoelastic coupling in $Fe_{1-x}Ga_x$ alloys [10,11]. In Fig. 5a, the calculated density of states shows that there is a pronounced non-bonding peak of Fe_2 atom near around Fermi level in contrast to the valley at the same energy range for Fe_1 atoms (Fe_1 atom shown in Fig. 1), indicating the broken Fe bond toward nearest Ga atoms. Due to the weak hybridization of Fe and Ga atoms, Fe bonds toward Ga atoms become dangling bonds and $d_{xz,yz}$ states shift in energy from the edge to the center of the 3d band, which reduces the total number of interlayer Fe–Fe bonds. As seen in Fig. 5b, for the schematic illustration of the atomic arrangement of $Fe_{1-x}Ga_x$ alloy at $x = 20.3\%$ in the $[1\bar{1}0]$ direction, The Fe–Fe bond is separated by a Fe–Ga mixed

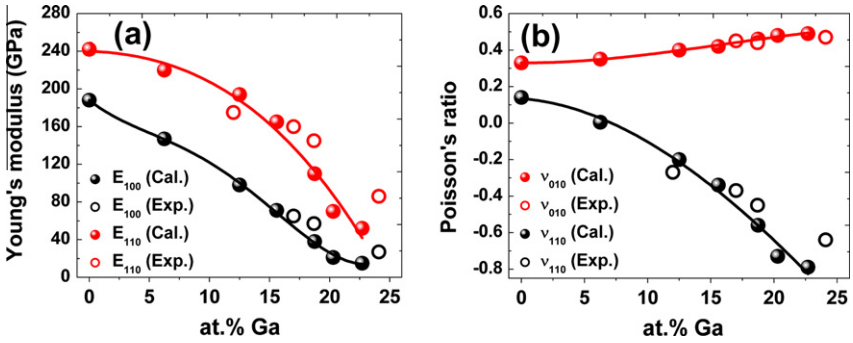

Fig. 4. Comparison between DFT simulation (filled symbols) and experimental data (open symbols) of (a) Young's modulus ($E_{[100]}$ and $E_{[110]}$) and (b) Poisson's ratio ($\nu_{[010]}$ and $\nu_{[110]}$) for $Fe_{1-x}Ga_x$ alloys.

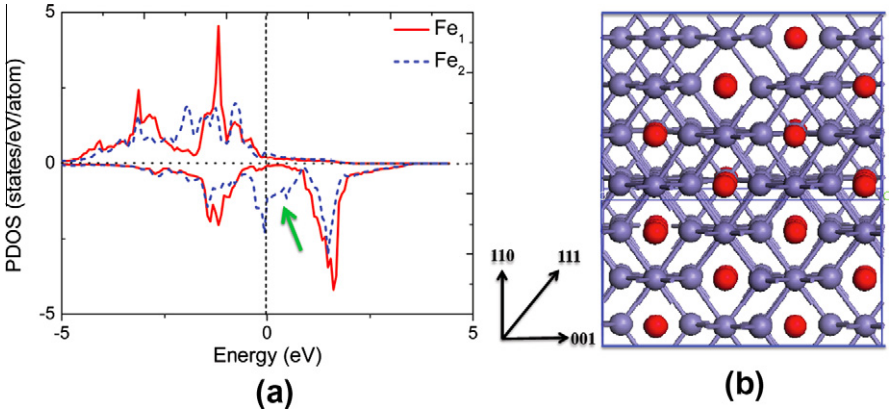

Fig. 5. (a) Partial density of states (PDOS) of Fe_1 and Fe_2 atoms for $Fe_{1-x}Ga_x$ alloys at $x = 20.3\%$ and (b) atomic configuration of $Fe_{1-x}Ga_x$ alloy at $x = 20.3\%$ viewed from $[1\bar{1}0]$ direction. The green arrow indicates the non-bonding states induced by Fe_2 atom.

layer in the [0 0 1] direction, which decreases the interaction between Fe–Fe layers. The Fe–Fe bond can hardly withstand stress if the stress is in the [0 0 1] direction, and will also cause a significant drop for the tetragonal shear modulus C' (Fig. 3a), while the ability to withstand stress in the [1 1 0] direction is obviously stronger because of the existence of more Fe–Fe bonds, as illustrated in Fig. 5b. This is also the reason why the Young's modulus in the [1 1 0] direction is larger than that in the [0 0 1] direction. The dependence of the Young's moduli in the [1 1 0] and [0 0 1] directions on the tetragonal shear modulus C' can be derived from Eqs. (7) and (8) as:

$$E_{[100]} = \frac{6C'B}{C_{11} + C_{12}} \tag{11}$$

and

$$E_{[110]} = \frac{4C_{44}}{1 + \frac{C_{44}}{3C'B}} \tag{12}$$

Since the rhombohedral shear modulus C_{44} (Fig. 3b) and bulk modulus B (doesn't show here) are almost constant for $Fe_{1-x}Ga_x$ at $15\% \leqslant x \leqslant 22.7\%$, the sharply decreased tetragonal shear modulus can be a primary factor for the low Young's modulus at high Ga concentrations (Fig. 4a). Meanwhile, with the introduction of the elastic anisotropy constant A ($A = 2C_{44}/(C_{11} - C_{12})$) [30], the Poisson's ratio $\nu_{[110]}$ in the [1 1 0] direction can be rewritten as:

$$\nu_{[110]} = \frac{1 - A\frac{C_{11}}{3B}}{1 + A\frac{C_{11}}{3B}} \tag{13}$$

Since the anisotropy constant A demonstrates a gradual increment at low Ga concentration and a burst at the Ga concentration $x = 15.6\%$ shown in Fig. 6 consistent with the experimental data [24,26], we may note that the sign change of the Poisson's ratio $\nu_{[110]}$ occurs when the anisotropy constant A is greater than 2, which is in agreement with the suggestion of Jain and Verma [31], who attributed the negative Poisson's ratio to materials exhibiting anisotropy constant larger than 2. Eq. (13) shows that the Poisson ratio in the [1 1 0] direction is negative when $A > 3B/C_{11}$ or $C' < C_{11}C_{44}/3B$. Therefore the drop of tetragonal shear modulus C' plays an important role for the decreased Poisson's ratio and final reach of large magnitude of the negative Poisson's ratio in the [1 1 0] direction (Fig. 4b). Such a large negative Poisson's ratio can exhibit a signifi-

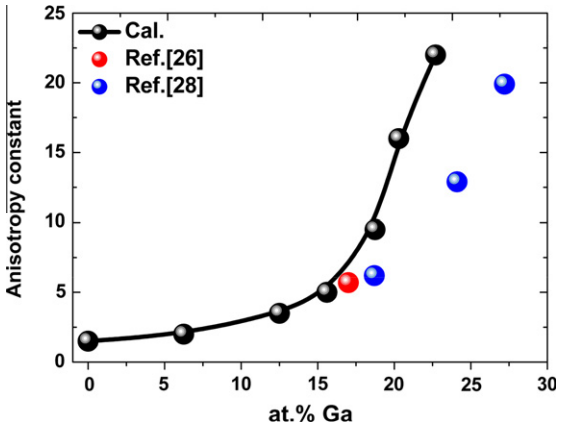

Fig. 6. DFT simulation and experimental data of dependence of anisotropic constant on the Ga concentration for $Fe_{1-x}Ga_x$ alloys.

cant in-plane auxetic response if the alloys are designed under specific loading conditions.

It is worth noting that the excellent ductility of $Fe_{1-x}Ga_x$ alloys can be further supported with both the classic criterion of the Cauchy pressure, defined as $(C_{12} - C_{44})$ [32], and the Pugh's modulus ratio G/B [33], where G and B are shear and bulk modulus, respectively. Previous studies also demonstrate the validity of studying ductile-to-brittle-transition in intermetallic compounds based on the above two criteria [34–39]. For metallic bonding, the Cauchy pressure is typically positive [32] and the Pugh's modulus ratio is less than 0.57 [33]. However, for directional covalent bonding with angular character, the Cauchy pressure is negative and the Pugh's modulus ratio is larger than 0.57. These correlations have been verified and validated [40–42] for typical metallic bond-based inductile materials (e.g. Au, Ag) as well as directional covalent bonding-based brittle materials (e.g. semiconductor Si, super-hard cubic BN, and diamond). From Fig. 7a, the Cauchy pressure $(C_{12} - C_{44})$ for $Fe_{1-x}Ga_x$ at all Ga concentration remains almost the same positive value, indicating a metallic bonding mechanism. The Pugh's modulus ratio G/B reflects the competition between the shear and cohesive strength at the crack tip of fracture. It is shown that all calculated G/B values are smaller than 0.57, demonstrating a ductile property from the Pugh's criterion. In order to clarify how good the ductility of $Fe_{1-x}Ga_x$ alloys is, we illustrated a few typical ductile materials of (Au, Ag), brittle material (Si), and super-hard materials (cubic BN and diamond) for comparison [40–42]. As shown in Fig. 7a, we can see that ductile Au and Ag locate in the upper left corner in relationship of $(C_{12} - C_{44})$ against G/B, while hard cubic BN and diamond almost lie in the bottom right corner. Unlikely, Fe and Si are almost close to the transitional edge of ductile-to-brittle transition. $Fe_{1-x}Ga_x$ alloys locate right between pure Ag and Fe, indicating an improved ductility with additional Ga in Fe. The inset of Fig. 7a explicitly shows a gradually increasing ductility of $Fe_{1-x}Ga_x$ alloys with increasing Ga concentration. Meanwhile, the relationship between $(C_{12} - C_{44})$ and G/B can be roughly fitted by quadratic curve for various Ga concentrations. To quantify a relationship of the ductile-to-brittle transition, we renormalized the Cauchy pressure $(C_{12} - C_{44})$ by dividing the Young's modulus E, and re-plotted the relationship of $(C_{12} - C_{44})/E$ vs. G/B based on the data in Fig. 7a. It is shown in Fig. 7b that $Fe_{1-x}Ga_x$ alloys at different Ga content can be fitted by a quadratic curve while the typical ductile and hard materials can be fitted by a hyperbola curve. As indicated by the arrow in Fig. 7b, the closer to the upper left corner, the more ductile and stronger metallic the bonding; inversely, the closer to the bottom right corner, the more brittle and stronger the covalent bonding. One may note that the value $(C_{12} - C_{44})/E$ of Ag is greater than that of $Fe_{1-x}Ga_x$ alloys (the highest Ga content studies here, depicted by the vertical black dot line in Fig. 7b), which implies that the metallic bonding of Ag is stronger than $Fe_{1-x}Ga_x$ alloys. It is also noted that the ductility of $Fe_{1-x}Ga_x$ alloys increases gradually with the Ga concentration and almost reaches the same G/B value as Ag, indi-

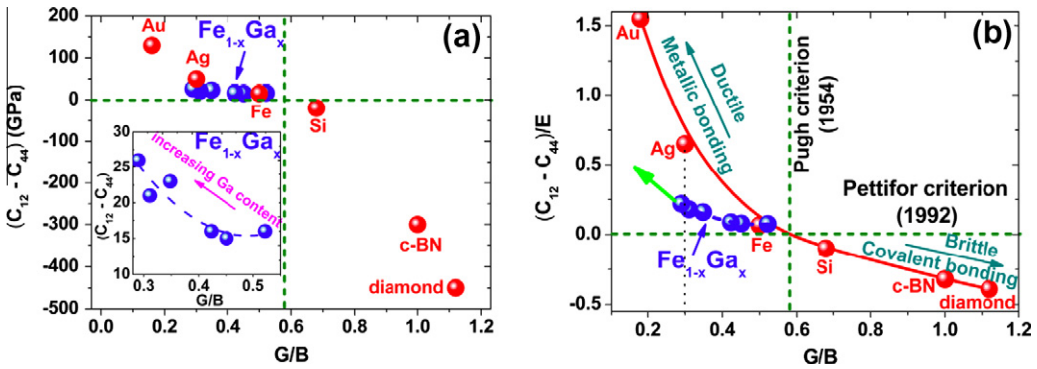

Fig. 7. (a) Correlation between the Cauchy pressure $(C_{12} - C_{44})$ (vertical axes) and the Pugh's modulus ratio G/B (horizontal axes) represented by blue ball for $Fe_{1-x}Ga_x$ alloys, along with typical ductile and hard materials for comparison depicted by red balls. The magnified correlation for $Fe_{1-x}Ga_x$ alloys at different Ga content was shown in the left bottom inset. (b) Renormalized hyperbolic correlation derived by dividing the Young modulus E from $(C_{12} - C_{44})$ for all the data of (a). The horizontal dashed line of $(C_{12} - C_{44})$ denotes the critical zero Cauchy pressure defined by Pettifor [32], whereas the vertical dashed line of $G/B = 0.57$ corresponds to the critical Pugh's modulus ratio defined by Pugh [33]. (For interpretation of the references to color in this figure legend, the reader is referred to the web version of this article.)

cating an excellent ductility as Ag, which plays a significant role in the enhancement of magnetostriction in these Fe–Ga alloys. It is expected that the ductility of $Fe_{1-x}Ga_x$ alloys can be further improved at even higher Ga concentration following the trend of quadratic relationship as depicted by the green arrow in Fig. 7b.

4. Concluding remarks

Based on the ab initio molecular dynamics (AIMD) results, different size-scaled cell models were constructed at different Ga concentration in order to systematically evaluate the anisotropic mechanical properties at Ga concentration, especially near the first magneostriction peak ($x = 19\%$). The calculated anisotropic shear constants $\acute{C}$ and C_{44} agree well with experimental data from different groups, which prove the validity and high quality of our calculations based on the supercell model. Meanwhile, the formation of $D0_3$-like structures has an important effect on the softness of tetragonal shear modulus and negligible influence on rhombohedral shear modulus. The decreasing Young's modulus and the large negative Poisson's ratio in the [1 1 0] direction can be attributed to the Fe dangling bond to its nearest Ga atoms. Moreover, the reason that the Young's modulus in the [1 1 0] direction is greater than in the [1 0 0] direction can be attributed to the different arrangement of the pure Fe layer and Fe–Ga mixed layer along the [1 1 0] and [1 0 0] axes. Furthermore, the ductility of $Fe_{1-x}Ga_x$ alloys was enhanced with increasing Ga content in terms of both classic Pettifor's Cauchy pressure $C_{12} - C_{44}$ and classic Pugh's modulus ratio G/B, which is significant for the enhanced magnetostriction at high Ga concentration.

Acknowledgements

This work was supported by CAS/SAFEA International Partnership Program for Creative Research Teams. HW and LZS acknowledge the support from NSF (Grant No: CMMI-0800417) and RQW acknowledges the support from ONR (Grant No: N00014-08-1-0143). Furthermore, ZDZ thanks the support from the National Natural Science Foundation of China (No. 50831006) and from the Ministry of Science and Technology of China National Basic Research Program (No. 2012CB619404). Computer simulations were conducted with the Shenyang Supercomputer Facility of Institute of Metal Research, Chinese Academy of Sciences and the US Department of Energy Supercomputer Facility.

References

[1] Clark AE, Restorff JB, Wun-Fogle M, Lograsso TA, Schlagel DL. IEEE Trans Magn 2000;36:3238.
[2] Clark AE, Wun-Fogle M, Restorff JB, Lograsso TA. IEEE Tran Magn 2001;37:2678.
[3] Cullen JR, Clark AE, Wun-Fogle M, Restorff JB, Lograsso TA. J Magn Magn Mater 2001;948:226.
[4] Clark AE. In: Wohlfarth EP, editor. Ferromagnetic materials, vol. 1. Amsterdam: North-Holland; 1980. p. 531.
[5] Andreev AV. In: Buschow KHJ, editor. Handbook of magnetic materials, vol. 8. Amsterdam: Elsevier; 1995. p. 59.
[6] Kainuma R, Imano1 Y, Ito W, Sutou Y, Morito H, Okamoto S, et al. Nature (London) 2006;439:957.
[7] Chmielus M, Zhang XX, Witherspoon C, Dunand DC, Müllner P. Nature Mater 2009;8:863.
[8] Atulasimha J, Flatau AB. Smart Mater Struct 2011;20:043001.
[9] Ikeda O, Kainuma R, Ohnuma H, Fukamichi K, Ishida K. J Alloys Compd 2002;347:198.
[10] Zhang YN, Cao JX, Wu RQ. Appl Phys Lett 2010;96:062508.
[11] Wang H, Zhang YN, Yang T, Zhang ZD, Sun LZ, Wu RQ. Appl Phys Lett 2010;97:262505.
[12] Wang H, Zhang YN, Wu RQ, Sun LZ, Xu DS, Zhang ZD. Manuscript in preparation.
[13] Xing Q, Du Y, McQueeney RJ, Lograsso TA. Acta Mater 2008;56:4536.
[14] Huang M, Mandru AO, Petculescu G, Clark AE, Wun-Fogle M, Lograsso TA. J Appl Phys 2010;107:09A920.
[15] Wuttig M, Dai L, Cullen J. Appl Phys Lett 2002;80:1135.
[16] Courtney TH. In: Mechanical behavior of materials. Boston, MA: McGraw-Hill; 2000. p. 56–61.
[17] Kohn W, Sham LJ. Phys Rev 1965;140(4A):A1133.
[18] Car R, Parrinello M. Phys Rev Lett 1985;55(22):2471.
[19] Marx D, Hutter J. In: Grotendorst J, editor. Modern methods and algorithms of quantum chemistry, NIC series, vol. 1. Jülich: John von Neumann Institute for Computing; 2000. p. 301–449.
[20] Kresse G, Hafner J. Phys Rev B 1994;49:14251.
[21] Perdew JP, Burke K, Ernzerhof M. Phys Rev Lett 1996;77:3865.
[22] Kresse G, Joubert D. Phys Rev B 1999;59:1758.
[23] Monkhorst HJ, Pack JD. Phys Rev B 1976;13:5188.
[24] Nye JF. Physical properties of crystals. Oxford: Clarendon; 1985.
[25] Kellogg RA, Russell AM, Lograsso TA, Flatau AB, Clark AE, Wun-Fogle M. Acta Mater 2004;52:5043.
[26] Clark AE, Hathaway KB, Wun-Fogle M, Restorff JB, Lograsso TA, Keppens VM, et al. J Appl Phys 2003;93:8621.
[27] Restorff JB, Wun-Fogle M, 1, Hathaway KB, Clark AE, Lograsso TA, et al. J Appl Phys 2012;111:023905.
[28] Xing Q, Lograsso TA. Appl Phys Lett 2008;93:182501.
[29] Petculescu G, Ledet KL, Huang M, Lograsso TA, Zhang YN, Wu RQ, et al. J Appl Phys 2011;109:07A904.
[30] Zhang YN, Wu RQ, Schurter HM, Flatau AB. J Appl Phys 2010;108:023513.
[31] Jain M, Verma MP. Indian J Pure Appl Phys 1990;28:178.
[32] Pettifor DG. Mater Sci Technol 1992;8:345.
[33] Pugh SF. Philos Mag 1954;45:823.
[34] Cottrel AH. Proc. European Conf. advanced materials and processes. Cambridge; 1991.
[35] Johnson RA. Phys Rev B 1998;37:3924.
[36] Pettifor DG, Cottrell AH. Electronis theory in alloy design farnham. UK: Ashgate Publishing; 1992.
[37] Chen K, Zhao L, Tse JS. J Appl Phys 2003;93:2414.
[38] Chen K, Zhao L, Tse JS. Phys Lett 2004;331:400.
[39] Niu HY, Chen XQ, Liu PT, Xing WW, Cheng XY, Li DZ, et al. Sci Rep 2012;2:718.
[40] Frederikse HPR. CRC Handbook of Chemistry and Physics. Elastic constants of single crystals. Boca Raton, FL: CRC Press; 2006.
[41] Connétable D, Thomas O. Phys Rev B 2009;79:094101.
[42] Yao HZ, Ouyang LZ, Ching WY. J Am Ceram Soc 2007;90:3194.